Research in Astronomy and Astrophysics, 23:085023 (14pp), 2023 August https://doi.org/10.1088/1674-4527/accb7f

A New Method of Frequency Fluctuation Estimation and IPS Processing Results Based on the Downlink Signal of Tianwen-1

Yu-Chen Liu[1,2], De-Qing Kong[1,2,*], Dong-Hao Liu[1,2], Xin-Ying Zhu[1,2], Yan Su[1,2], Hong-Bo Zhang[1,2], and Zan Wang[1,2]

[1] Key Laboratory of Lunar and Deep Space Exploration, National Astronomical Observatories, Chinese Academy of Sciences, Beijing 100101, China; kdq@bao.ac.cn

[2] University of Chinese Academy of Sciences, Beijing 100049, China

Received 2023 January 19; revised 2023 March 22; accepted 2023 March 23; published 2023 July 10

Abstract

The radio-occultation observations taken by Tianwen-1 are aiming to study the properties of solar wind. A new method of frequency fluctuation (FF) estimation is presented for processing the down-link signals of Tianwen-1 during the occultation period to study the properties of the coronal plasma at the heliocentric distances of 4.48–19 $R_\odot$. Because of low S/N as well as the phase fluctuation phenomena caused by solar activity, a Kalman based on polynomial prediction methods is proposed to avoid the phase locked loop loss lock. A new detrend method based on multi-level iteration correction is proposed to estimate Doppler shift to get more accurate power density spectra of FF in the low frequency region. The data analyze procedure is used to get the properties of the solar corona during the occultation. The method was finally verified at the point when the solar offset is 5.7 $R_\odot$, frequency tracking was successfully performed on data with a carrier-to-noise ratio of about 28 dBHz. The density spectra obtained by the improved method are basically the same when the frequency is greater than 2 mHz, the uncertainty in the result of the rms of the FF obtained by removing the trend term with different order polynomials is less than 3.3%. The data without eliminating interference show a large error for different detrending orders, which justifies the need for an improved approach. Finally, the frequency fluctuation results combined with the information on intensity fluctuation obtained by the new method are compared with the results of the integrated Space Weather Analysis system and theoretical formula, which verifies that the processing results in this paper have a certain degree of credibility.

Key words: methods: data analysis – Sun: corona – Sun: heliosphere – (Sun:) solar wind – Physical Data and Processes

1. Introduction

Interplanetary scintillation (IPS) refers to electromagnetic wave signals that are affected by the activity of the outer coronal plasma layer of the Sun that they pass through, thus exhibiting rapid changes in parameters such as angle of arrival, amplitude, and phase (Xu & Song 2019).

Early IPS research mainly used natural radio sources (Hewish 1955; Hewish et al. 1964) to invert the characteristics of the Sun. However, natural radio sources can only provide information on amplitude scintillation, the use of electromagnetic waves emitted by deep space detectors to conduct IPS experiments can further explore the structure of the corona by using the frequency fluctuation (FF), group delay, and Faraday rotation of the signal. In the late 1960s, Goldstein studied the relationship between spectral broadening and overall electron density in the coronal region using data from Mariner-4, the first spacecraft to successfully fly by Mars, and later Mariner-6 (Goldstein 1969). In terms of Doppler measurements, Berman and Wackley used Pioneer 10, 11 and Helios 1 data in 1975 to show that Doppler scintillation is a good way to study solar wind disturbances (Berman & Wackley 1976), Berman further showed in 1981 that the mean fluctuation of the Doppler data is proportional to the total electron density (Berman et al. 1982). Research by Woo (1988) and Woo & Armstrong (1992) showed that Doppler scintillation is not only affected by heliocentric distance, but the dynamic solar wind also causes instantaneous scintillation in Doppler data. By comparing experiments with plasma measurements, Woo et al. (1985) found that interplanetary shocks are generally responsible for this instantaneous scintillation during periods of high solar activity, while Doppler scintillation is sometimes caused by co-rotating particle streams during periods of low solar activity.

Scintillation research during the radio occultation period has always been a common concern of the communication field and the astronomical community. Through the study of interplanetary scintillation, more information on the physical parameters of the solar wind can be obtained. On the other hand, it is of great scientific significance to study and understand the Sun-terrestrial space environment to provide a guarantee for the stable operation of deep space probes.

At the beginning of this century, a series of IPS studies were also carried out in China (Zhu et al. 2012; Liu et al. 2021),

---

[*] Corresponding author.

which were all based on ground observation settings to observe natural radio sources. With the successful launch of the Tianwen-1 deep space probe and the advancement of more deep space missions, it is urgent to establish a systematic data processing method for IPS research using deep space probes. A few months ago, scientists used VLBI methods, combined with Mars Express and Tianwen-1 data, to probe the solar corona (Ma et al. 2022). Similar efforts have been carried out by researchers in the past decade, and their methods have been applied to such as Messenger (Wexler et al. 2019a), Mars Express (Bocanegra-Bahamón et al. 2018; Ma et al. 2021), Akatsuki (Wexler et al. 2020a; Chiba et al. 2022) and other missions. The inversion of solar parameters has achieved good results. On the basis of them, this paper proposes an improved data processing method for calculating more accurate phase scintillation information based on the characteristics of the Tianwen-1 detector signal.

In Section 2, two schemes based on median filtering to improve the accuracy of frequency estimation in deep space exploration in highly dynamic environments are proposed, which have different purposes but similar principles. In Section 2.2, when the Phase-Locked-Loop (PLL) may lose lock under high dynamic noise, a judgment of interference of PLL based on Multi-Level Iteration Correction (MLIC) is proposed, so that the PLL can be assisted by Kalman filter to track Doppler frequency when the loop is at the edge of out-of-lock, thereby eliminating the tracking error of phase-locked loops due to high dynamics and eliminates the wild value. In Section 2.3, based on the previous outlier judgment scheme, a new method is proposed to fit the long-period slow trend of frequency that results in more accurate frequency residuals for analysis of solar activity. In Section 3, the above two schemes are verified with the real data from Tianwen-1, and the accuracy of the results is compared.

2. Method of Frequency Fluctuation Estimation

2.1. The Characteristics of the Downlink Data

The downlink data received from Tianwen-1 are transmitted by medium gain antenna in the X-band, during superior conjunction of the Mars over solar offset (SO) range from 4.5 to 19 $R_\odot$(solar radii), which defined as the distance from the proximate point to the heliocenter. In order to obtain the phase scintillation (Doppler scintillation) information of the signal, the one-way Doppler measurement mode is adopted (Zheng 2013), which means after the satellite transmits the beacon signal of the nominal frequency, the ground radio telescope completes the signal reception and frequency measurement. The single-station single-frequency measurement mode was adopted in this experiment. However, the weak signal transmitted from a medium gain antenna and the strong interference from the inner solar wind bring difficulties in frequency measurement. Figure 1 shows the spectrogram of the Tianwen-1 downlink signal received by the Wuqing 70 m radio telescope (WRT70) on 2021 October 12.

Costas loop is used to obtain the instantaneous frequency (Zheng 2013; Buccino et al. 2018), and after deducting the long-time varying trend caused by the relative motion between the satellite and Earth, we obtain the residual frequency which provides the information on solar activity. In view of the characteristics of low signal-to-noise ratio (S/N) and large scintillation of downlink data, this section will propose some new methods suitable for processing Frequency Fluctuation data for a single station.

We observe density fluctuations using electromagnetic signals traversing the Sun’s corona, which are mainly affected by the proximate point on the line of sight (LOS). The signal frequency observed at the receiver system, $f_{\rm obs}$, has the following relationship with the original transmitted frequency f_0 (Pätzold et al. 2016; Wexler et al. 2019b)

$$f_{\rm obs}\,(t) = f_0 - \frac{V_{\rm rel}(t)}{c} f_0 + \frac{1}{2\pi} r_e \lambda \frac{d}{dt} \int_{\rm Earth}^{\rm Tianwen-1} n_e(s,\,t) ds, \tag{1}$$

where $\lambda = c/f_0$ is the transmitted carrier frequency, c is the speed of light, n_e is the electron number density function with respect to the LOS integration path s and time t, and r_e is the classical electron radius which equals to 2.82×10^{-15} m.

The second term in Equation (1), $-f_0 V_{\rm rel}/c$, is the Doppler frequency shift, which comes from the relative velocity, $V_{\rm rel}$, between the detector and the Earth receiving station, which usually manifests as a long-period slow motion of the signal (Ma et al. 2021). The method of eliminating the long period will affect subsequent frequency fluctuations spectral power estimation, especially causing fitting errors in the low-frequency part (Wexler et al. 2020a). In the past, there are mainly two processing methods to remove the gradual change caused by relative motion, which are direct polynomial fitting and the ephemeris method. The literature Wexler et al. (2020a) proposes using a third-order polynomial to fit the data every 4000 s to eliminate long periods. Ma et al. (2021) use a higher-order polynomial for fitting, and compare the method of using the satellite ephemeris to eliminate the period. It is found that the errors caused by the two methods are concentrated below 3 mHz. However, for the data of this study, neither simple polynomial fitting nor ephemeris can provide a solution precise enough.

Because the local Doppler data sometimes has a large scintillation, it will lead to the polynomial long-period fitting affected by the local jump, and the error of eliminating the period will be brought about. For Mars exploration, the computational complexity of ephemeris is very high, and the accuracy of calculating relative motion through ephemeris is affected by the long distance, long delay, and complex relative motion in deep space (probe autonomous orbit adjustment, Mars revolution, Earth Rotation), many effects lead to high

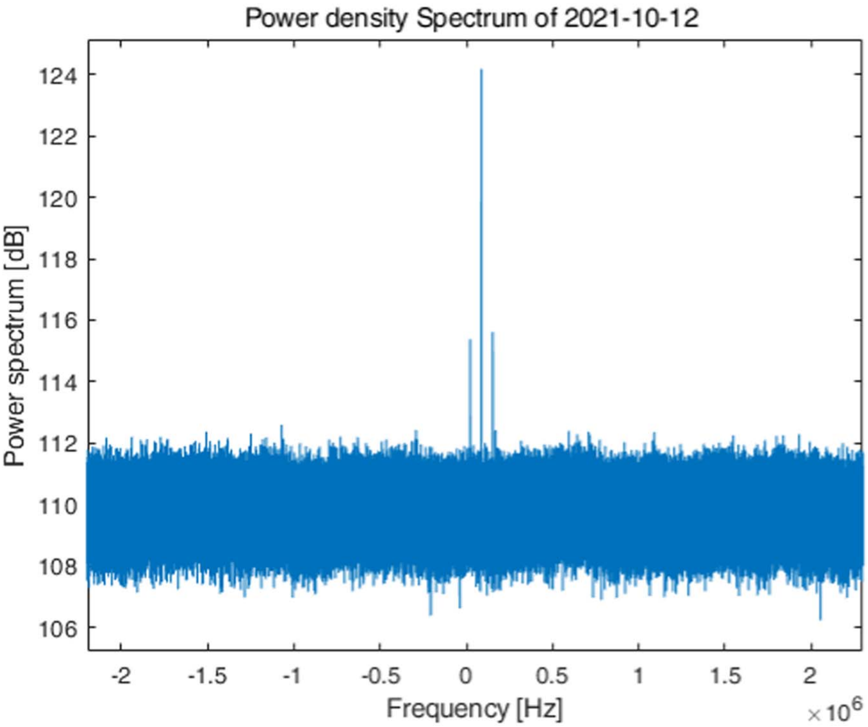

Figure 1. Power density spectra for Tianwen-1 at WRT70 at 08:02:09 when $R_\odot = 5.7$. The sampling rate is 6.25 MHz with 8 bit digitized, integration time is 32 s, spectral resolution is 5.96 Hz. It can be seen that due to the Doppler shift, the frequency point of the signal is not at zero.

computational complexity, and this also means that the Doppler scintillation data cannot be processed immediately and accurately when the downlink data obtained. After removing the slow motion of the signal, we can obtain the instantaneous signal changes, so as to further study the influence of the solar corona on the signal.

$$\delta f(t) = f_{\text{obs}}(t) - \left[f_0 + \frac{V_{\text{rel}}(t)}{c} f_0\right] = \frac{1}{2\pi} r_e \lambda \frac{d}{dt} \int_{\text{Earth}}^{\text{Tianwen}-1} n_e(s, t) dS \tag{2}$$

Fluctuation variance σ_{FF}^2 is defined to infer the number density fluctuation information based on the numerical integration of FF spectral density over frequency limits [ν_{lo}, ν_{up}]. (Wexler et al. 2019b)

$$\sigma_{\text{FF}}^2 = \int_{\nu_{\text{lo}}}^{\nu_{\text{up}}} |\mathcal{F}\{\delta f(t)\}|^2 d\nu, \tag{3}$$

where $\mathcal{F}\{...\}$ represents the Fourier Transform. The lower frequency limit of the FF spectral integration ν_{lo} is affected by the length of observation and the detrending method. In previous work (Ma et al. 2021), it was found that the effect of the detrending term on the results above 3 mHz was negligible. The upper limit ν_{up} required to below the Nyquist frequency and noise floor (Wexler et al. 2020a).

The digital PLL (Molera Calvés 2012; Yuldashev 2013; Buccino et al. 2018) is used to estimate the instantaneous frequency and phase. When phase-locking is successful, the Doppler frequency estimated by the PLL has a strong long-period trend with time. For the phase disturbance record of the Cassini satellite in 2000 (Morabito et al. 2003), the frequency shift is on a second scale and the long-time regularity presented is not caused by the disturbance of the solar wind. This is mainly caused by the influence of the relative motion of the earth. In order to obtain the information on the solar activity, that is, the third information of Equation (1), it is necessary to remove the slow change caused by the relative motion of the aircraft, which is a quasi-sine wave shape on the long-period scale. After the long-period slow change is eliminated, the residual frequency reflecting the influence of the solar wind can be obtained.

To this end, we proposed a long-period fitting method based on multi-level iteration correction and denoising to eliminate the long-period error of the signal.

2.2. PLL Tracking Based on Adaptive Filtering

In the field of deep space exploration, especially during the occultation period, solar activity has a great influence on Doppler measurements, so that the effect of solar activity can cause instability of the PLL. The PLL-based closed-loop parameter estimator is a classical frequency phase estimation method (Gardner 2005; Molera Calvés 2012; Buccino et al. 2018; Deng et al. 2021). Due to the harsh conditions of the down-link narrow-band signal of deep space detection, it is easy to have a low S/N of the received signal and a dynamic frequency variation beyond the allowable range of the PLL, resulting in serious problems such as the inability to track, loss of lock, and large parameter estimation error (Paik & Asmar 2011).

In order to solve the problem of frequency jump and loss of lock of PLL under solar activity, the following frequency estimation and tracking structure is proposed in Figure 2.

The data processing flow is divided into two working modes, Frequency Tracking Mode and Frequency Correction Mode, switching depends on whether the PLL is at the edge of out-of-lock. Under normal conditions, enter the Frequency Tracking Mode. In this mode, the initial frequency offset due to the Doppler effect is first estimated by the Fast Fourier Transform (FFT), and then the estimated value of the initial frequency offset is used as a priori condition to assist the locking of the PLL and get the estimated Doppler frequency. At the same time, the estimated frequency offset obtained after the PLL is used as feedback to assist the subsequent frequency tracking. Through the interference detection of the output results from the PLL which will discuss in Section 2.2.2, if the solar wind causes relatively large frequency scintillation to break the loop of PLL, the Frequency Correction Mode is entered, and the Doppler frequency is predicted and the instantaneous frequency is corrected by the Kalman filter.

2.2.1. Frequency Tracking Mode based on PLL

The down-link narrow-band signal transmitted by the deep space probe received by the ground receiving station, the signal after down-converted with sampling rate f_s are $s(n)$, which can be expressed as

$$s(n) = a(n)\cos\left[2\pi f(n)/f_s + \varphi(n)\right], \tag{4}$$

where $f(n) = \delta f(n) + f_c + f_d$ and $\varphi(n)$ are the instantaneous received frequency and phase changing in time, and f_c is the frequency at which the spacecraft transmits signals, f_d is the Doppler frequency, $a(n)$ is the modulated information of signal.

The received signal multiplied by the cosine signal output by the numerically controlled oscillator (NCO) can be expressed as (Yuldashev 2013)

$$\begin{aligned} I(n) &= a(n)\cos\left[2\pi f(n)/f_s + \varphi(n)\right]\cos\left[2\pi f_{\rm est}(n)/f_s + \tilde{\varphi}(n)\right] \\ &= \frac{1}{2}a(n)\cos\left[2\pi\Delta f(n)/f_s + \Delta\varphi(n)\right] \\ &\quad \times \cos\left[2\pi(f(n) + f_{\rm est}(n))/f_s + \varphi(n) + \tilde{\varphi}(n)\right], \end{aligned} \tag{5}$$

where $f_{\rm est}(n)$ and $\tilde{\varphi}(n)$ are the estimation of instantaneous frequency and phase.

After low-pass filtering, it can be obtained, where $\Delta f = f(n) - f_{\rm est}$, and $\Delta\varphi(n) = \varphi(n) - \tilde{\varphi}(n)$

$$I'(n) = \frac{1}{2}a(n)\cos\left[2\pi\Delta f(n)/f_s + \Delta\varphi(n)\right]. \tag{6}$$

The same can be obtained

$$Q'(n) = \frac{1}{2}a(n)\sin\left[2\pi\Delta f(n)/f_s + \Delta\varphi(n)\right]. \tag{7}$$

Multiplied as the phase detector result $\Upsilon(n) = I'(n)Q'(n) \approx \frac{1}{4}a^2(n)[2\pi\Delta f(n)/f_s + \Delta\varphi(n)]$.

The status iteration of digital second-order PLL in the nth data-frame can be expressed as follows to get the estimation of instantaneous frequency $f_{\rm est}$(Buccino et al. 2018)

$$\begin{cases} f_{\rm est}(n) = f_{\rm est}(n-1) + (C_1 + C_2)\Upsilon(n) - C_2\Upsilon(n-1) \\ f_{\rm d}(n) = f_{\rm est}(n) - C_1\Upsilon(n) \\ \tilde{\varphi}(n) = \Upsilon(n-1) + 2\pi f_{\rm est}(n)/f_s \end{cases} \tag{8}$$

Here C_1 and C_2 are the loop parameters of the PLL (Gardner 2005), which usually obtained based on actual situation and experience. $\tilde{\varphi}(n)$ is the numerically controlled oscillator (NCO), $f_{\rm d}(n)$ is the Doppler frequency estimation.

With the initial condition

$$\begin{cases} f_{\rm est}(0) = f_{\rm ini} \\ \Upsilon(0) = 0 \\ f_{\rm d}(0) = 0 \\ \tilde{\varphi}(0) = 0 \end{cases} \tag{9}$$

The rough estimation of initial Doppler frequency $f_{\rm ini}$ can be calculated by FFT (Molera Calvés 2012), with the resolution as $\Delta f_{\rm FFT} = f_s/N_{\rm FFT}$, where $N_{\rm FFT}$ is the number of FFT counts points. The accuracy of the initial frequency estimation affects the capture time required before the phase-locked loop enters the tracking state.

2.2.2. Interference Detection

The movement of the deep space detector can be described as follows without considering the extreme situations such as EDL (Entry, Descent, and Landing) (Paik & Asmar 2011; Niu et al. 2014), the Doppler frequency $f_{\rm d}(t)$ can be represented as (Qi et al. 2020)

$$\begin{aligned} f_{\rm d}(t_k) &= f_{\rm d}(t_{k-1}) + f_{\rm d}^{(1)}(t_{k-1})\Delta t + \frac{f_{\rm d}^{(2)}(t_{k-1})}{2!}\Delta t^2 \\ &\quad + \cdots \frac{f_{\rm d}^{(n)}(t_{k-1})}{n!}\Delta t^n + O(\Delta t^{n+1}), \end{aligned} \tag{10}$$

where $t \in [t_0, t_0 + T)$. When the satellite is in normal working condition, the slow change of the Doppler frequency at the receiver for a long time can be fitted by order-p polynomials ${}^{p}f_{\rm trend}(n)$ for a relatively long time interval from time $n - M$ to

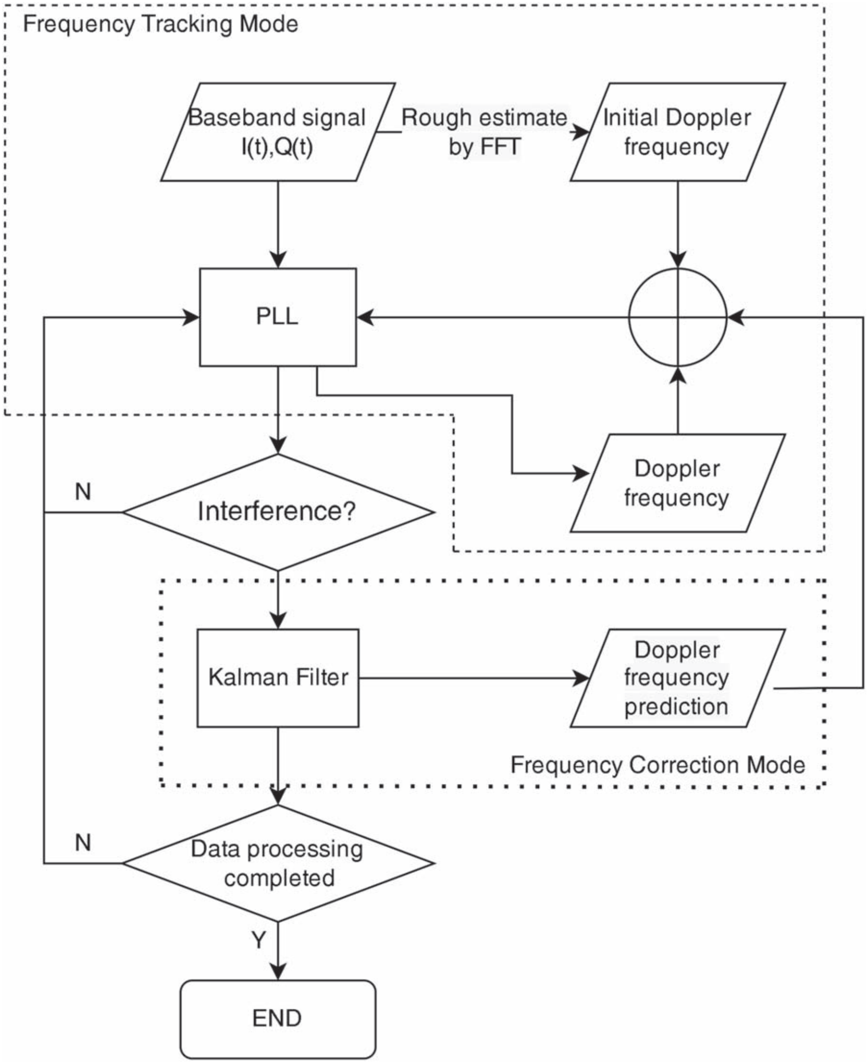

Figure 2. Flow chart of the frequency estimation algorithm.

current time n.

$$\begin{bmatrix} t_{n-M+1}^{0} & t_{n-M+1}^{1} & t_{n-M+1}^{2} & \cdots & t_{n-M+1}^{p} \\ t_{n-M+2}^{0} & t_{n-M+2}^{1} & t_{n-M+2}^{2} & \cdots & t_{n-M+2}^{p} \\ \vdots & \vdots & \vdots & \ddots & \vdots \\ t_{n}^{0} & t_{n}^{1} & t_{n}^{2} & \cdots & t_{n}^{p} \end{bmatrix} \begin{bmatrix} a_0 \\ a_1 \\ \vdots \\ a_p \end{bmatrix} + \begin{bmatrix} \epsilon_{n-M+1} \\ \epsilon_{n-M+2} \\ \vdots \\ \epsilon_n \end{bmatrix} = \begin{bmatrix} {}^{p}f_{\text{trend}}(n-M+1) \\ {}^{p}f_{\text{trend}}(n-M+2) \\ \vdots \\ {}^{p}f_{\text{trend}}(n) \end{bmatrix} \tag{11}$$

Let

$$\min_{a} \epsilon^{T}\epsilon \tag{12}$$

to get ${}^{p}f_{\text{trend}}(n)$, where $\boldsymbol{a} = [a_0, a_1, \ldots, a_p]^T$ and $\epsilon = [\epsilon_{n-M+1}, \epsilon_{n-M+2}, \ldots, \epsilon_n]^T$.

The solar scintillation effects, especially at the superior conjunction period, will cause out of lock of PLL. The intuitive manifestation of the loss of lock of the PLL is that it leads to a frequency jump in f_{d} compared to ${}^{p}f_{\text{trend}}$. Therefore, the problem of detecting interference of PLL can be transformed into finding out the abnormal moment t when $f_{\text{res}}(n) = f_{\text{est}}(n) - {}^{p}f_{\text{trend}}(n)$ deviates from the mean relatively large, where

$$f_{\text{res}}(n) = \begin{cases} f_{\text{d}}(n), & n - M > 0 \\ f_{\text{d}}(n) - {}^{p}f_{\text{trend}}(n), & \text{otherwise} \end{cases} \tag{13}$$

Since the S/N of the return signal during superior conjunction of the Mars is extremely low, in order to improve

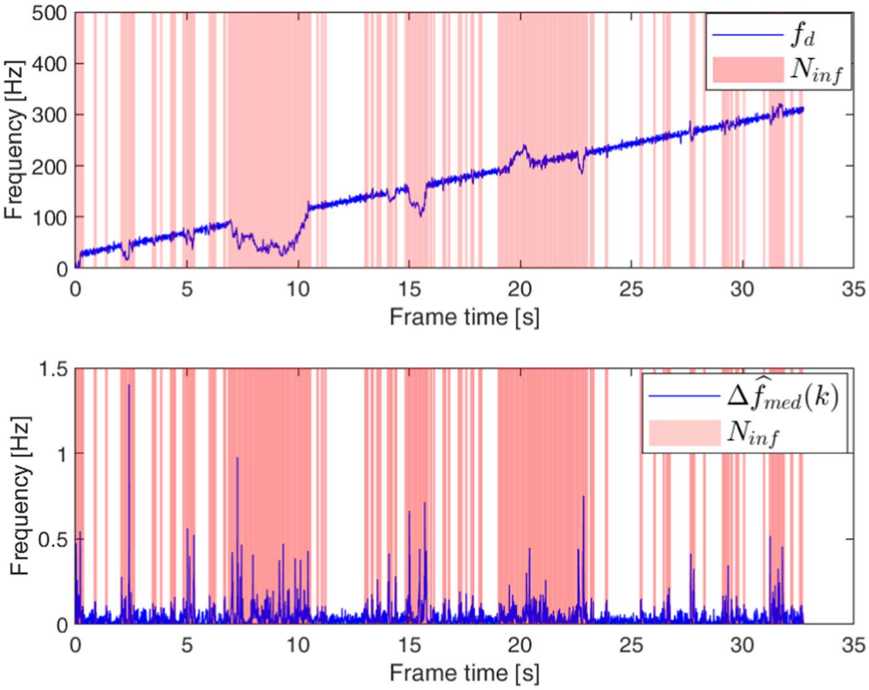

Figure 3. The comparison of $\Delta\widehat{f}_{\text{med}}(k)$ and the abnormal points in f_{d}. The shaded areas in red represent the intervals detected as points of interference.

the S/N of the signal and simplify the subsequent calculations, we integrate the Doppler data. Without losing its generality, every j data have been integrated at the current time i.

$$f_{\text{sum}}(i) = \sum_{k=i-j+1}^{i} f_{\text{res}}(k). \tag{14}$$

Then perform median filtering on $f_{\text{sum}}(i)$

$$\widehat{f}_{\text{med}}(i) = \begin{cases} \text{median}[\widetilde{f}_{\text{sum}}(i-(m-1)/2\text{: } i+(m-1)/2)], & m \text{ is odd} \\ \text{median}[\widetilde{f}_{\text{sum}}(i-m/2\text{: } i-1+m/2)], & m \text{ is even} \end{cases} \tag{15}$$

and

$$\widetilde{f}_{\text{sum}}(i) = \begin{cases} f_{\text{sum}}(i), & i \in [0, k] \\ 0, & \text{else} \end{cases} \tag{16}$$

where k represents the current moment. In order to determine whether there are jittering disturbing points in the Doppler, we make a difference between the results after median filtering to get the difference of amplitude

$$\Delta\widehat{f}_{\text{med}}(k) = \widehat{f}_{\text{med}}(k) - \widehat{f}_{\text{med}}(k-1). \tag{17}$$

A piece of data from 2021 October 12 is taken as an example to plot Figure 3, which clearly shows the correspondence between the magnitude of $\Delta\widehat{f}_{\text{med}}$ and the anomaly caused by the instability of PLL. Then a threshold α can be set to determine the extent to which solar activity affects Doppler frequency tracking. The initial value of threshold α can be set as a value slightly less than the average value of $\Delta\widehat{f}_{\text{med}}$, and then the result of Equation (22) is used instead of the initial value of α. If the result $\Delta\widehat{f}_{\text{med}}$ is less than the threshold α, the abnormal scintillation is considered to be absent at this time. Then the Frequency Tracking Mode is still working as before. Otherwise, if $\Delta\widehat{f}_{\text{med}}(k) > \alpha$, the loop enters the Frequency Correction Mode in Section 2.2.3.

However, the above operation is based on the assumption that the polynomial fitting results ${}^{p}f_{\text{trend}}(t)$ of the time interval t to $t-T$ is accurate at the moment t. In fact, Doppler estimation f_{d} during the upper conjunction period is greatly affected by the instantaneous activity of the solar wind, and Figure 3 shows the resulting jumps in frequency estimation that inevitably affect the accuracy of fitting trends directly using polynomials. In Figure 4(a), the error in estimating the trend term caused by direct polynomial fitting (the green line in Figure 4(a)) can be seen visually. At the same time, this is bound to affect the determination of interference points discussed above.

In order to make the trend estimation results of polynomial fitting ${}^{p}f_{\text{trend}}$ fit the real long-term change trend, an improvement scheme of multi-level iteration correction is proposed in the following. For illustrative purposes, let us assume that the discrete numerical coordinates corresponding to the time from $t-T$ to t are $k=1$ to $k=M$. In order to eliminate the jump interference point, a suitable threshold is required. We adopted

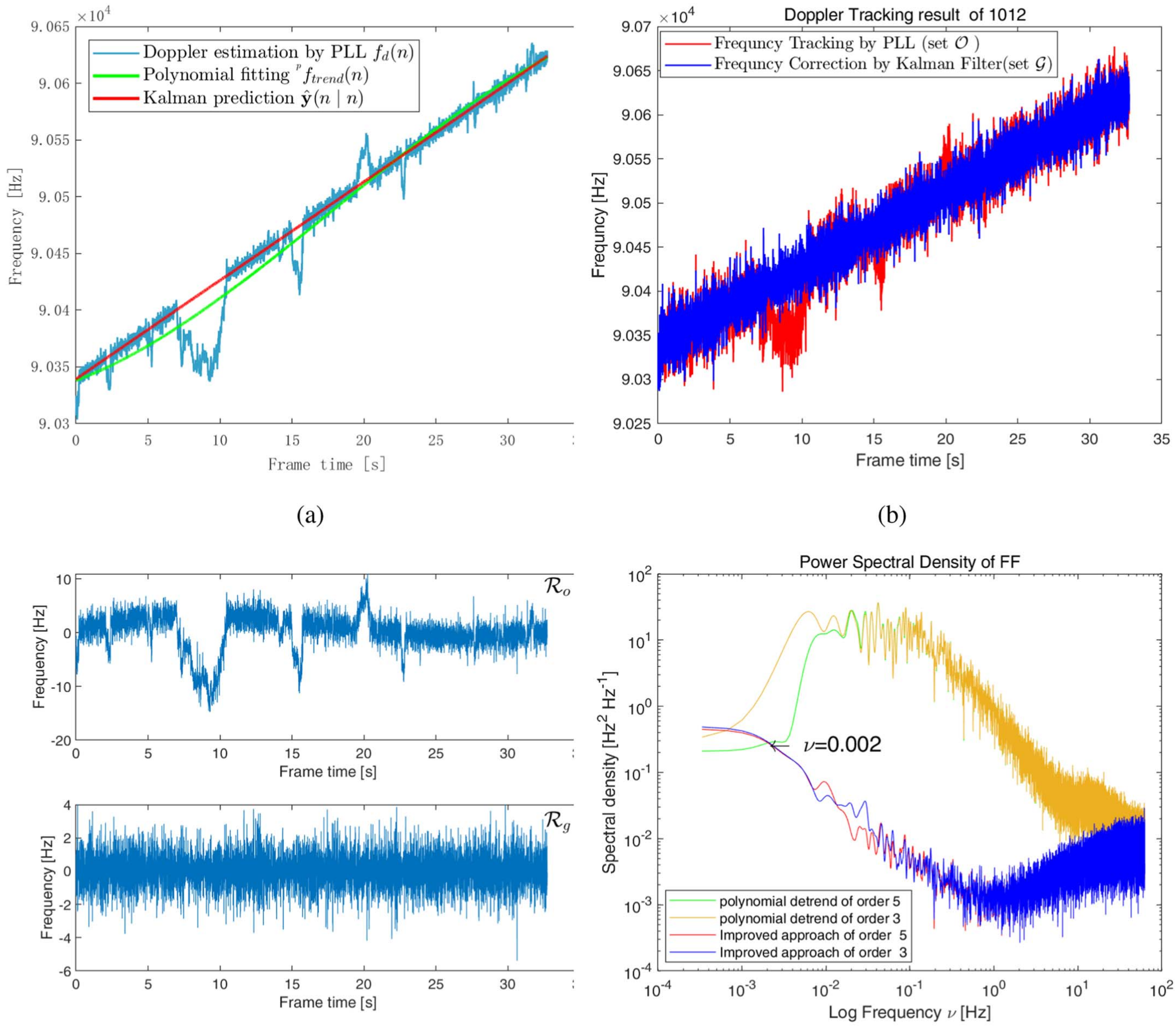

(a) (b)

(c) (d)

Figure 4. Frequency residuals extracting process (a) Comparison of traditional detrending method and the Kalman filter to predict Doppler shift. (b) Prediction performance of the Medfilt-based Kalman filter. (c) Comparison after different detrend methods. The upper one corresponds to the time domain diagram obtained after the direct polynomial detrend method (set ${}^p\mathcal{R}_o$) of order 5. The lower figure is the time domain diagram using the new approach (set ${}^p\mathcal{R}_g$) with $p = 5$. (d) This is the plot of FF spectral density. The green line and yellow line in the figure are the spectral density deduced from ${}^5\mathcal{R}_o$ and ${}^3\mathcal{R}_o$, while red and blue line are calculated by ${}^5\mathcal{R}_g$ and ${}^3\mathcal{R}_g$.

a multi-level iteration method to set the threshold. To eliminate interference points, the process of the m^{th} time is as follows:

(1) *Find average.* To eliminate larger amplitude values, the average is calculated as

$$\mu_m = \frac{1}{M - \underline{\mathrm{card}}\, H_{m-1}} \sum_{k=1, k \notin H_{m-1}}^{M} \Delta f_{\mathrm{med}}(k), \tag{18}$$

where μ_m is the estimation mean value of the difference of amplitude $\{\Delta f_{\mathrm{med}}(k)\}_{k=1}^{M}$, $\underline{\mathrm{card}}\, H_{m-1}$ is the amount of the elements in H_{m-1}, and

$$H_{m-1} = \bigcup_{q=0}^{m-1} F_q. \tag{19}$$

F_q is the set of frequency point $k_{q,i}$ of the interference signal detected by the q-level interference detection module. And

$$F_q = \{k_{q,i}\},\ q \neq 0,\ i = 1,\ 2,\cdots,\ \underline{\text{card }}F_q \tag{20}$$

especially, define $F_0 = \phi$ when $q = 0$.

(2) *Calculate variance.* In the second step, find the variance of the amplitude difference

$$\sigma_m = \sqrt{\frac{1}{M - \underline{\text{ card }}H_{m-1}} \sum_{k=1, k \notin H_{m-1}}^{M} (\Delta f_{\text{med}} - \mu_m)^2}\,. \tag{21}$$

(3) *Determine interference via threshold.* This article decides to set the threshold to the following form

$$Q_m = \mu_m + \alpha_m \sigma_m. \tag{22}$$

When $\Delta f_{\text{med}}(k) \geqslant Q_m$, the corresponding k can be calculated. Assume that there are L's value that meets the above conditions, to represent as $\{k_{\text{i}}\}_{\text{i}=1}^{L}$.

(4) *Delete interference and their neighbor.* For our purpose, the interference points, which are caused by the effect of loss of lock of PLL, do not occur in isolation. Therefore, a neighborhood of the interference points should be chose to delete.

$$N_{\text{inf}} = \{k\,|\,|k - k_l| \leqslant n,\ k_l \in \{k_{\text{i}}\}_{\text{i}=1}^{L}\} \tag{23}$$

(5) *Polynomial fitting.* The order-p polynomial fit is used to detrend the remaining points $\{f_{\text{est}}(k)\}_{k \notin N_{\text{inf}}}$ and the corresponding time $\{t_{\text{est}}(k)\}_{k \notin N_{\text{inf}}}$. We suppose the result after iterative correction is ${}^{p}f'_{\text{trend}}(k)$.

We will use actual data in Section 3 of the following article to illustrate that the error of polynomial fitting curves of different orders p obtained by using the iterative correction method ${}^{p}f'_{\text{trend}}(k)$ (p generally selected between order 3 and 10 (Ma et al. 2021)) is much smaller than that of the traditional direct fitting. Or it can be said that the ${}^{p}f'_{\text{trend}}(k)$ obtained by the new method is not sensitive to the selection of order-p. In fact, we will show in Section 3 that the error of different p for subsequent parameter inversion is less than 3.3%.

The importance of the iterative correction method in this interference detection module is to ensure the accurate identification of interference points. After accurate judgment, the loop enters the Frequency Correction Mode to be described below.

2.2.3. Frequency Correction Mode Based on Kalman Filter

The adaptive method filters out the out-of-lock effect of PLL to ensure tracking. Kalman filtering based on the median filter was introduced to ensure the tracking of the loop under extreme conditions.

We introduce Kalman filtering into the PLL to denote the state equation and observation equation as follows

$$\begin{cases} \boldsymbol{y}(k) = \boldsymbol{G}\boldsymbol{y}(k-1) + \boldsymbol{W}(k-1) \\ \boldsymbol{z}(k) = \boldsymbol{H}(k)\boldsymbol{y}(k) + \boldsymbol{V}(k) \end{cases} \tag{24}$$

where the observation value $\boldsymbol{z}(k)$ is taken to be ${}^{p}f'_{\text{trend}}(k)$ that calculated in Section 2.2.2, $\boldsymbol{H}(k)$, $\boldsymbol{V}(k)$ are the observation vector, measurement matrix and observation noise at time k. Transmission matrix, measurement matrix and state vector are respectively

$$\boldsymbol{G} = \begin{bmatrix} 1 & T & T^2/2 \\ 0 & 1 & T \\ 0 & 0 & 1 \end{bmatrix}$$

$$\boldsymbol{H} = [1 \ \ 0 \ \ 0]^T$$

$$\boldsymbol{y}(k) = \left[\, f_{\text{d}}(t_k) \ \ f''_{\text{d}}(t_k) \ \ f'{}'_{\text{d}}(t_k) \right]^T \tag{25}$$

and

$$\boldsymbol{S}(n) = \boldsymbol{E}[\text{W}(n)\text{W}^H(n)]$$

$$\boldsymbol{R}(n) = \boldsymbol{E}[V(n)V^H(n)] \tag{26}$$

The new Doppler frequency estimation can be given by the following algorithm (Niu et al. 2014; Qi et al. 2020)

$$\text{for} \quad k = 1,\ 2,\ldots,N \tag{27}$$

$$\hat{\boldsymbol{y}}(k|k-1) = \boldsymbol{G}\hat{\boldsymbol{y}}(k-1|k-1)$$

$$\boldsymbol{P}(k|k-1) = \boldsymbol{G}\boldsymbol{P}(k-1|k-1)\boldsymbol{G}^H + \boldsymbol{K}(k-1) \tag{28}$$

$$\boldsymbol{K}(\text{k}) = \boldsymbol{P}(k|k-1)\boldsymbol{H}(k)^T(\boldsymbol{H}(k)\boldsymbol{P}(k|k-1)\boldsymbol{H}(k)^T + \boldsymbol{R}(k))^{-1} \tag{29}$$

$$\boldsymbol{\alpha}(k) = \boldsymbol{z}(k) - \boldsymbol{H}(k)\hat{\boldsymbol{y}}(k|k-1) \tag{30}$$

$$\hat{\boldsymbol{y}}(k|k) = \hat{\boldsymbol{y}}(k|k-1) + \boldsymbol{K}(k)\alpha(k) \tag{31}$$

$$\boldsymbol{P}(k|k) = [\boldsymbol{I} - \boldsymbol{K}(k)\boldsymbol{H}(k)]\boldsymbol{P}(k|k-1) \tag{32}$$

with the initial condition

$$\hat{\boldsymbol{y}}(0|0) = \hat{\boldsymbol{y}}(0) = [\,{}^{p}f'_{\text{trend}}(k_0),\ ({}^{p}f'_{\text{trend}}(k_0) - {}^{p}f'_{\text{trend}}(k_0 - \Delta t))/\Delta t,\ 0]^T \tag{33}$$

Replace the frequency value of the k-th cycle in Equation (8) with the Kalman filter value as follows.

$$\begin{cases} f_{\text{est}}(k) = \psi(k-1) + (C_1 + C_2)\Upsilon(k) - C_1\Upsilon(k-1) \\ f_{\text{d}}(k) = \hat{\boldsymbol{y}}(k|k) \\ f_{\text{correc}}(k) = f_{\text{d}}(k) + C_1\Upsilon(k) \\ \tilde{\varphi}(k) = \Upsilon(k-1) + 2\pi f_{\text{est}}(k)/f_s\,. \end{cases} \tag{34}$$

Then we can get the result of frequency correction $f_{\text{correc}}(t_k)$, which is an estimation of $f_{\text{est}}(t_k)$ based on the result of the previous cycle of PLL, or frequency correction after suppressing Doppler frequency jump caused by instability of PLL. The total result of frequency tracking that achieves the purpose of suppressing out-of-lock effects of PLL on Doppler frequency estimation can be expressed as

$$\mathcal{G} = \{f_{\text{est}}(k)\}_{k \notin N_{\text{inf}}} \bigcup \{f_{\text{correc}}(k)\}_{k \in N_{\text{inf}}}. \tag{35}$$

For the convenience of the following article, the traditional tracking results without out-of-lock effects suppression can be listed, where we can define the range of the observation time set $\mathcal{T}_{\text{obs}}$.

$$\mathcal{O} = \{f_{\text{est}}(k)\}_{k \in \mathcal{T}_{\text{obs}}}. \tag{36}$$

2.3. Long-period Detrending Based on Multi-level Iteration Correction

In the previous section, this article introduced a signal processing method to suppress frequency jump due to loss of stabilization of PLL at a low S/N and obtained a set of frequency estimation results $\mathcal{G}$ with wild value eliminated.

After removing the interference caused by the phase-locked loop, the next step is to eliminate the long-period trend of the time series. As it had been discussed in Equation (2), the effective information of solar activity is not related to the long-period variation of the Doppler frequency due to the movement of the satellite. The task in extracting solar activity parameters is to efficiently obtain the residuals after removing the trend term. The traditional method of removing trend terms is to remove the direct polynomial fitting introduced in previous Section 2.2.2, and there is also a method of removing the residuals using ephemeris (Ma et al. 2021). In general, in the case of near-Earth satellites, ephemeris fitting is a method that can be considered, but for remote-distance, multi-planetary motion coupled deep space exploration, this method not only cannot process the latest data in real-time but also brings excessive calculations.

In this section, we propose a new method to detrend the long-trend term. For convenience, the Doppler frequency offset data in $\mathcal{G}$ may be recorded as $\{f_{\text{est(k)}}\}_{k=1}^{N}$, and the corresponding time frame is $\{t_{\text{obs}}(k)\}_{k=1}^{N}$. This section is treated as an afterthought, so the fit of the trend term ${}^{p}f_{\text{trend}}$ differs from the previous section. At this point, just replace Equation (11) with the form below. For the convenience of formula representation, it is assumed that M is odd, and if M is even, it does not affect subsequent conclusions

$$\begin{bmatrix} t^0_{n-(M-1)/2} & t^1_{n-(M-1)/2} & \cdots & t^p_{n-(M-1)/2} \\ \vdots & \vdots & \ddots & \vdots \\ t^0_n & t^1_n & \cdots & t^p_n \\ \vdots & \vdots & \ddots & \vdots \\ t^0_{n+(M-1)/2} & t^1_{n+(M-1)/2} & \cdots & t^p_{n+(M-1)/2} \end{bmatrix} \begin{bmatrix} a_0 \\ a_1 \\ \vdots \\ a_p \end{bmatrix} + \begin{bmatrix} \epsilon_{n-(M-1)/2} \\ \vdots \\ \epsilon_n \\ \vdots \\ \epsilon_{n+(M-1)/2} \end{bmatrix} = \begin{bmatrix} {}^{p}f_{\text{trend}}(n-(M-1)/2) \\ \vdots \\ {}^{p}f_{\text{trend}}(n) \\ \vdots \\ {}^{p}f_{\text{trend}}(n+(M-1)/2) \end{bmatrix} \tag{37}$$

Since the S/N of the return signal during superior conjunction of the Mars is extremely low, in order to improve the S/N of the signal and simplify the subsequent calculations, we integrate the Doppler data as before, where integrate every k_{num} data

$$f_{\text{sum}}(i) = \sum_{k=(i-1)k_{\text{num}}+1}^{i \cdot k_{\text{num}}} f_{\text{est}}(k) - f_{\text{trend}}(k). \tag{38}$$

Then a median filter was performed on the integrated Doppler data $f_{\text{sum}}(i)$ as in Equation (12).

Because the operation at this time is not limited to the information at the current moment as in Section 2, $\widetilde{f}_{\text{sum}}$ in Equation (16) becomes

$$\widetilde{f}_{\text{sum}}(i) = \begin{cases} f_{\text{sum}}(i),\ i \in [0, N/k_{\text{num}}] \\ 0, \text{ else} \end{cases} \tag{39}$$

where N is the largest time point in the observation set $\mathcal{T}_{\text{obs}}$.

Referring to the operation of Equation (17) filtering the interference point, we get Δf_{med}. It is important to note that although the formula is identical, the previous Δf_{med} is based on the result of the current moment k derived only from the information at the previous moment, and the Δf_{med} in this section is the result based on the global information. So now the judgment will be more accurate.

The larger value of Δf_{med} corresponds to the frequency value of jumping after being affected by coupling of solar wind and loss of lock of PLL. As introduced in Section 2.2.2, these jump values will affect the accuracy of the subsequent long-term fitting.

With the above symbols defined within the scope of this section, the algorithm required next is exactly the same as described in Section 2.2.2. When ${}^{p}f'_{\text{trend}}(k)$ is obtained, only the difference is needed to obtain the frequency residuals used to analyze solar activity

$${}^{p}\mathcal{R}_g = \{f_{\text{est}}(k) - {}^{p}f'_{\text{trend}}(k)\}_{f_{\text{est}} \in \mathcal{G},\, k \in \mathcal{T}_{\text{obs}}}. \tag{40}$$

Similarly, the frequency residuals deduced by traditional method can be expressed as

$${}^{p}\mathcal{R}_o = \{f_{\text{est}}(k) - {}^{p}f_{\text{trend}}(k)\}_{f_{\text{est}} \in \mathcal{O},\, k \in \mathcal{T}_{\text{obs}}}. \tag{41}$$

3. Result and Test

An extensive series of interplanetary scintillation (IPS) observations was made by Tianwen-1 down-link signals during the superior solar conjunction of Mars over solar offset range 4.48–19 $R_\odot$ in 2021.

To test the effectiveness of the proposed method, we choose the downlink data on 2021 October 12 from 07:59:00 ~ 10:00:00 (UTC) as the experimental data when the SO value is $5.7R_\odot$, which is in the middle corona region (from 1.5 to 6 $R_\odot$ (Wexler et al. 2022)). The signal is observed at X-band and received by the Wuqing 70 m radio telescope (WRT70) that sampled at the rate of 6.25MHz with 8 bit digitized, and the phase locking bandwidth is set to be 20 Hz.

Figure 1 is the power density spectra for Tianwen-1 at 08:02 on October 12.

3.1. Frequency Fluctuation Data

In order to visually illustrate the previous processing method, we selected a data processing result of about 33 s which starts at 8:07:38 to draw Figures 4(a)–(c). Figure 4(a) is the comparative verification of the long period elimination method based on multi-level iteration correction proposed in Sections 2.2 and 2.3. The blue line in Figure 4(a) is the Doppler frequency estimation f_{d} made only by PLL without correction. The green line in the figure is the result of the traditional direct use of polynomial fitting, where the order of fitting is taken to be $p = 5$. It can be clearly seen that the traditional direct fitting will cause the distortion of the fitting trend due to the jitter of the instantaneous frequency. The red line in the figure is the result of $\hat{\boldsymbol{y}}(k|k)$ in Equation (34). Even in the case of severe jitter, the Doppler trend can be well estimated.

Figure 4(b) can well show the comparison between the frequency tracking result of the classic PLL method (set $\mathcal{O}$) and the result processed by the algorithm in this paper(set $\mathcal{G}$). The red line in this figure is the frequency tracking result of the original PLL. It can be seen that due to the close distance from the Sun ($\mathrm{SO} = 5.7R_{\odot}$), the frequency estimation is affected by the activity of the solar corona, and the jitter occur at the same time. The blue line is the advanced Tracking method discussed in Section 2.2. It can be clearly seen that the improved processing method greatly improves the stability of frequency tracking.

Figure 4(c) is a time domain plot of frequency residuals obtained using two different data processing methods, and its time coordinates are the same as the previous two figures. The figure above is the frequency residuals obtained by subtracting the directly fitting trend term represented by the green line, in Figure 4(a), from the instantaneous frequency tracking result that has not been corrected by the Kalman filter, that is the set ${}^{p}\mathcal{R}_{o}$ with $p = 5$. It can be observed that the slow trend term is not completely removed when the frequency jump is large. And the frequency jumps generated in the PLL are not entirely affected by the signal as it passes through the solar corona. The frequency jumping in the upper Figure 4(c) for up to several seconds is a loss of lock due to the properties of the loop when tracking a highly dynamic target (Gardner 2005). The lower time domain plot is obtained by using the Kalman filter to compensate for the frequency jump, that is the set ${}^{p}\mathcal{R}_{g}$ with $p = 5$. At this time, the method of detrending is also more refined. And before the trend term is fitted, there is a disturbance point of frequency jump after the median filtering, which is the method represented by the red line in Figure 4(a).

Figure 4(d) is a comparison of frequency fluctuation power spectra plotted with data of about 3000 s. The process of plotting the power spectrum can be found in the work of previous (Imamura et al. 2005; Wexler 2020b). In this figure, we not only add the comparison of two different detrend schemes (the green and red line) add, but also make a comparison of the fitting results of the scheme under different orders (the red and blue line). It can be seen that compared with the traditional long-period fitting scheme, the result of the improved method is not sensitive to the fitting order. In order to accurately estimate the electron spectral density (Ma et al. 2021), the trend fitting scheme proposed is very necessary. For the improved approach, the spectra are almost the same when $\nu \geqslant 2$ mHz. In terms of accuracy, it is 1 mHz higher than the work of previous (Ma et al. 2021).

The large perturbation of the Doppler data in Figures 4(c) and (d) is due to the coupling of solar atmospheric activity with the PLL out-of-lock effect.

These disturbances affect the elimination of long-term trends in the data, resulting in subsequent calculations of the error of the electron density spectrum in the low-frequency range.

Once the long-time trend term is removed and the frequency residuals are obtained, we can calculate the FF spectral density. The methods taken to calculate the frequency fluctuation spectra are described by Imamura et al. (2005). Chiba et al. (2022) study the frequency fluctuation spectra by taking 2000 s sub-intervals per day with a resolution of 1.31 s using Akatasuki data detecting the heliocentric distance of 1.5–8.9 $R_{\odot}$. Bruno et al. (2009) point out that the time resolution of frequency fluctuation to study the FF spectra is just required to be smaller than the local ion gyro-period with enough long time duration compared with the period (Bruno & Carbone 2013). Taking into account the effective observation time and the amount of calculation afterward, 3000 s time segment and 0.1 s time resolution is used. (See Figure 4(d)).

After obtaining the FF Spectral spectrum, we select the same upper and lower integral limits (1–28 milliHz (mHz) band for $\sigma_{\mathrm{FF1}}^{2}$ and 0.5–100 mHz band for $\sigma_{\mathrm{FF2}}^{2}$, and $\sigma_{\mathrm{FF}}^{2} = (\sigma_{\mathrm{FF1}}^{2} + \sigma_{\mathrm{FF2}}^{2})/2$) consistent with earlier research (Wexler 2020b) to calculate fluctuation variance σ_{FF}^{2} by Equation (3). The radio wavelength-normalized rms frequency fluctuation measure σ_{FM} was defined as follows, and the uncertainty was estimated to be half of the difference between FF of the narrow and wide frequency bands (Wexler et al. 2020a)

$$\sigma_{\mathrm{FM}} = \frac{\sqrt{\sigma_{\mathrm{FF}}^{2}}}{\lambda} \tag{42}$$

where λ is the radio transmitter wavelength in meter which is X-band here, r is the SO value in solar radii. The fluctuation variance σ_{FM} that based on different methods, which shows in Figure 4(d), are listed in Table 1 (Wexler et al. 2020a).

It can be seen that the data processed with the new detrending method is not sensitive to the order of the fit, while the traditional method is the opposite. The new method uses two different fitted orders to obtain σ_{FM} with an uncertainty of

Table 1
Information Deduced from the FF Spectral Density on 2021 October 12 from 08:00 to 08:50 (UTC)

	Method	$\sigma^2_{\rm FFJ}$ Hz^2	$\sigma_{\rm FM}$ Hz m^{-1}
Data with interference	${}^5\mathcal{R}_o$	26.2818 ± 16.0198	112.1142 ± 89.7319
Data with interference	${}^3\mathcal{R}_o$	29.1425 ± 18.9657	121.9877 ± 89.3588
Improved Approach	${}^5\mathcal{R}_g$	$(3.5753 \pm 3.1029) \times 10^{-4}$	0.4934 ± 0.1925
Improved Approach	${}^3\mathcal{R}_g$	$(3.8802 \pm 3.3183) \times 10^{-4}$	0.5103 ± 0.2100

Note. The SO of the observing interval on October 12 is about 5.7 $R_\odot$.

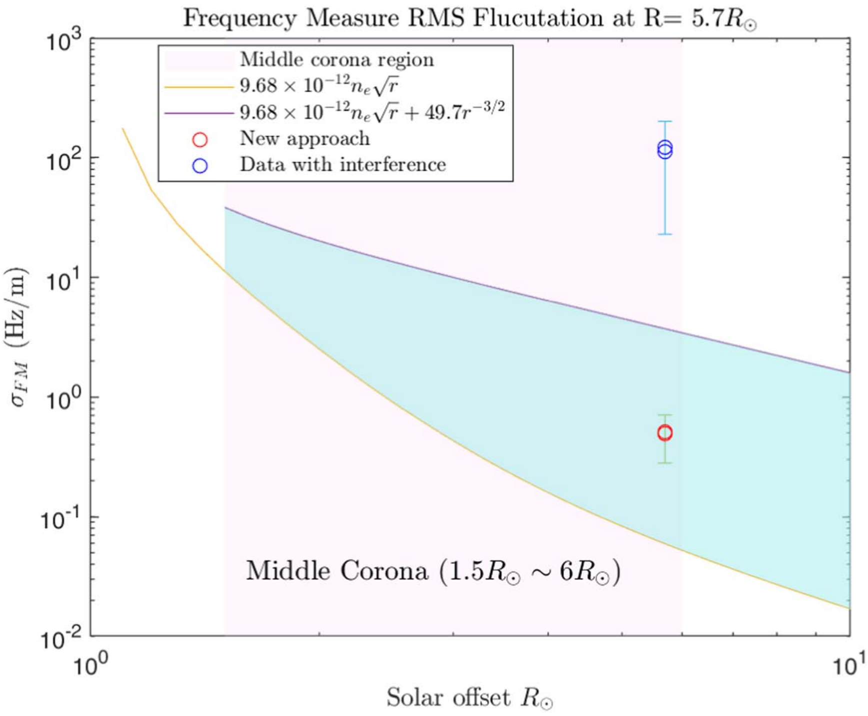

Figure 5. Frequency measure fluctuation results. Areas shaded in pink represent the extent of the middle coronal. Equation (44) and a correction from Equation (45) for the information on solar wind speed surrounding the shaded area of light blue. The two dots in red are the result of detrending by different orders using the improved method, and the maximum uncertainty is chosen. Similarly, the blue dots represent the results obtained by data with interference.

less than 3.3% of the electron number density compared to 8.8% in a traditional way.

The electron number density N_e can be calculated from the empirical model (Wexler et al. 2019a) under the assumption of average case of slow wind circumstance

$$n_e = \left[\frac{65}{r^{5.94}} + \frac{0.678}{(r-1)^{2.25}}\right] \times 10^{12} \qquad [\mathrm{m}^{-3}]. \qquad (43)$$

Then, we can calculate the theoretical plasma density on 2021 October 12 , which is $2.5716 \times 10^{10}\ \mathrm{m}^{-3}$. During periods of calmer solar activity, an interpretation of FF in the inner part of the middle corona for given n_e is proposed by Wexler et al. (2022)

$$\sigma_{\rm FM} = 9.69 \times 10^{-12} n_e \sqrt{r} \qquad (44)$$

A term incorporates information of solar wind outflow speed is added for larger SO

$$\sigma_{\rm FM} = 9.69 \times 10^{-12} n_e \sqrt{r} + 49.7 r^{-3.2}. \qquad (45)$$

Figure 5 shows these two curves and the rms frequency fluctuation results $\sigma_{\rm FM}$ obtained using different methods.

The figure once again verifies that for the improved method, the detrending of different orders has little effect on the results, which almost coincide. While for the traditional method, the difference can be seen. The results obtained by improving the method are consistent with the theoretical formula.

The results with interference are much larger than the theoretical value. But Wexler et al. (2020a) also suggest that if there were the presence of coronal mass ejection (CME), the rms frequency fluctuation measure σ_{FM} would be much larger than the theoretical value predicted by Equation (45). We will verify in the next section that the solar wind outflow speed at that time meets the conditions for low speed, which excludes the possibility of CME.

3.2. Comparative Analysis of Intensity Scintillation Data

In order to verify the premise of the formula in the previous section, the case of the quiet solar wind, we combine the information reveals by intensity scintillation to get the inversion of the solar wind properties. We apply a similar data reduction and processing procedure for single station single frequency (SSSF) given by Liu et al. (2021) to get the intensity power spectral (see Figure 6(a)), the integration time is 1ms with a length of ≈100 s.

Under the weak-scattering assumption, the intensity scintillation spectrum can be expressed as follows (Scott et al. 1983; Liu et al. 2021; Chiba et al. 2022)

$$P(f;\, V,\, \alpha,\, \mathrm{AR},\, s_i) = \frac{2\pi(\lambda r_{\mathrm{e}})^2}{V}\int_{-\infty}^{\infty}\Phi_1(f;\, q_y,\, V,\, \alpha,\, \mathrm{AR}) \times \Phi_2(f;\, q_y,\, V,\, s_i)F_{\mathrm{diff}}(f;\, q_y,\, V)\mathrm{d}q_y, \tag{46}$$

where r_e is the classical electron radius and λ is the observing wavelength which is determined as we use the single X-band for our experiment. V is the component of solar wind velocity perpendicular to the LOS.

In Equation (46), the electron density spectrum Φ_1 is in direct proportion to $q^{-\alpha}$, where $q = \sqrt{q_x^2 + q_y^2}$ is the two-dimensional wavenumber. $q_x = 2\pi f/V$. Φ_2 is related to the inner scale s_i that describes the scale at which the turbulence dissipates (Scott et al. 1983; Chiba et al. 2022).

The Fresnel propagation filter F_{diff} is acting as a high-pass filter that attenuates wavenumber below the Fresnel spatial frequency $q_F = \sqrt{\lambda z/(4\pi)}$.

To fit the theoretical intensity scintillation spectra, L-BFGS (Limited-memory Broyden–Fletcher–Goldfarb–Shanno) method is applied to obtain the global optimal (Chiba et al. 2022). The accuracy of the measurement of solar wind speed and other three parameters will suffer selection effects during the fitting process of SSSF (Zhang 2007). Since the parameter AR and s_i mainly affect the slope between Fresnel knee and noise floor (Scott et al. 1983), on the basis of previous research (Liu et al. 2021; Chiba et al. 2022), we added new optimization goals to the model fitting of SSSF

$$\begin{cases} \min\sum_{i=1}^{N} W(i)||\log(P(V,\, \alpha,\, \mathrm{AR},\, s_i)) - \log(P_{\mathrm{obs}})||^2 \\ \min||K_{\mathrm{theory}}(\mathrm{AR},\, s_i) - K_{\mathrm{obs}}||^2 \end{cases} \tag{47}$$

where W is the weight and K is the inclined rate between Fresnel knee and the noise floor.

We compare the solar activity parameters based on the inversion of intensity (Figure 6(a)) and frequency scintillation (Figure 6(b)) on 2021 October 12 with the interplanetary observations of that day (Figure 6(c)) provide by NASA's the Integrated Space Weather Analysis System(iSWA). According to iSWA's, the speed of the solar wind at about 06:57 on 2021 October 12 is low. However, iSWA's observations can only indicate that solar activity was relatively quiet at the interplanetary scale (1 au $\approx 215 R_\odot$), which could not provide the speed of the solar wind in the middle corona region. The activity of the solar middle corona was also relatively calm at that time is the only information that can be inferred. The inversion of solar wind velocity from intensity scintillation is the radial component of the outflow velocity, approximately at 80 km s^{-1}, which consists of iSWA's model and empirical values at such SO (Wexler et al. 2020a), and better reflects the calm state of the solar activity. Therefore, the conditions at that time make the empirical Equations (43), (44) and (45) valid. This result illustrates the effectiveness of the treatment method proposed in this paper.

4. Conclusion and Prospect

In this paper, a systematic Doppler frequency measurement method for Mars exploration missions and its application to the estimation of solar activity region parameters are proposed. The main conclusions are:

1. A scheme of frequency tracking and correction is proposed in the presence of high dynamic Doppler noise (such as Sun noise) in the deep space communication scene. In the actual test when SO is less than 6 $R_\odot$, X-band, rapid changes in frequency were successfully tracked by PLL.
2. In order to measure the electron density fluctuation spectrum in the LOS direction by using the Doppler scintillation data of spacecraft radio, a more effective long-period elimination scheme is proposed, which is verified to correct the error of the frequency scintillation spectrum in the low frequency band, the uncertainty of estimating σ_{FM} improves from 8.8% to 3.3%. This increases the accuracy trusted in the lower frequency limit of power spectrum integration ν_{lo} to 2 mHz.
3. Using the inversion method of intensity scintillation combined with NASA's observations, it was determined

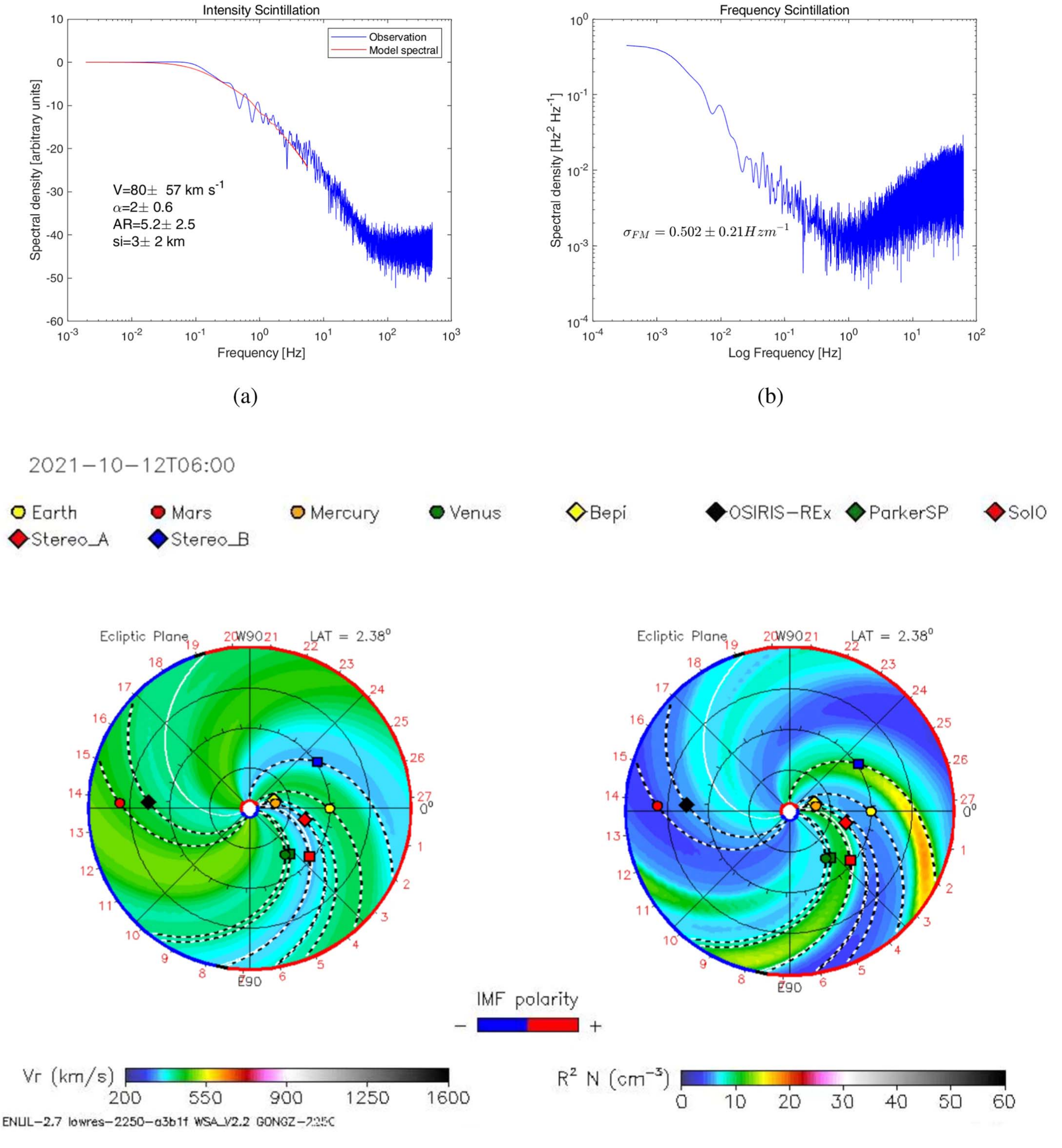

(a)

(b)

(c)

Figure 6. The Interplanetary plasma properties for the time of our observations (2021 October 12 at 06:57 UTC). (a) Intensity scintillation spectrum and its corresponding model inversion. (b) Frequency scintillation spectrum obtained by the new detrend approach in this paper. (c) (Right) Electron density content times the square of the radial distance from the Sun [N(cm^{-3})]. (Left) Solar wind radial speed on the elliptic plane in km s^{-1}. It can be seen that the solar activity at that time was relatively calm. Simulations are available through the Integrated Space Weather Analysis System (iSWA, https://ccmc.gsfc.nasa.gov/iswa/).

that the Sun was in a relatively calm state around 8:00 a. m. on 2021 October 12. However, iSWAs data can only provide information at the interplanetary scale (1 au $\approx 215 R_{\odot}$). In order to obtain the parameters of the solar corona, the paper combines with intensity scintillation data to reflect the results of the quiet solar wind, verifying the relatively calm state of the solar corona during observation. Thus, it can be verified that the results obtained by the improved method are consistent with the theoretical values.

This paper verifies the advantages of the improved method for calculating FF, and verifies that the results are consistent with the theoretical values, and that in the middle coronal, the frequency is affected by $n_e \sqrt{r}$ and $r^{-3.2}$. The second of these represents the effects of the low-speed solar wind. The use of intensity scintillation data can just reflect the information on solar wind speed, thereby improving the credibility and accuracy of the fitting. In the next step, we will use the improvements proposed in this paper to make an overall statistical analysis of the data during the Tianwen-1 occultation period.

Acknowledgments

This work was funded by the Astronomical Joint Fund of the National Natural Science Foundation of China and Chinese Academy of Sciences (Grant Nos. U1831114, 11941002, and 12073048).

References

Berman, A. L., & Wackley, J. A. 1976, The Deep Space Network Progress Report, 42-33, 159

Berman, A. L., Wackley, J. A., & Hietzke, W. H. 1982, TDA Progress Report, 42-71, 117

Bocanegra-Bahamón, T. M., Molera Calvés, G., Gurvits, L. I., et al. 2018, A&A, 609, A59

Bruno, R., & Carbone, V. 2013, LRSP, 10, 2

Bruno, R., Carbone, V., Vörös, Z., et al. 2009, EM&P, 104, 101

Buccino, D. R., Kahan, D. S., Yang, O., & Oudrhiri, K. 2018, USNC-URSI NRSM 2018, 1 (Boulder, CO: IEEE)

Chiba, S., Imamura, T., Tokumaru, M., et al. 2022, SoPh, 297, 34

Deng, T., Ma, M.-L., Liu, Q.-H., & Wu, Y.-J. 2021, RAA, 21, 221

Gardner, F. M. 2005, Phaselock Techniques (3rd edn.; Hoboken, NJ: Wiley)

Goldstein, R. M. 1969, Sci, 166, 598

Hewish, A. 1955, RSPSA, 228, 238

Hewish, A., Scott, P. F., & Wills, D. 1964, Natur, 203, 1214

Imamura, T., Noguchi, K., Nabatov, A., et al. 2005, A&A, 439, 1165

Liu, L.-J., Peng, B., Yu, L., et al. 2021, MNRAS, 504, 5437

Ma, M.-L., Molera Calvés, G., Cimò, G., et al. 2021, AJ, 162, 141

Ma, M.-L., Molera Calvés, G., Cimò, G., et al. 2022, ApJL, 940, L32

Molera Calvés, G. 2012, Aalto Univ., 216

Morabito, D. D., Shambayati, S., Finley, S., & Fort, D. 2003, ITAP, 51-2, 201

Niu, G.-Q., Yan, Y., Li, Y.-C., et al. 2014, 4th IMCCC 2014 (Harbin: IEEE), 533

Paik, M., & Asmar, S. W. 2011, IEEEP, 99, 881

Pätzold, M., Häusler, B., Tyler, G. L., et al. 2016, P&SS, 127, 44

Qi, H.-T., Zhang, X.-L., & Zhu, L.-J. 2020, Chinese Space Science and Technology, 40, 19

Scott, S., Coles, W., & Bourgois, G. 1983, A&A, 123, 207

Wexler, D. 2020b, Ph.D. thesis., Toowoomba, AU: Univ. of Southern Queensland On the Fluctuations of Electron Density and Magnetic Field in the Solar Mid-Corona: Space Radio Observations

Wexler, D. B., Hollweg, J. V., Efimov, A. I., et al. 2019a, ApJ, 871, 202

Wexler, D. B., Hollweg, J. V., Efimov, A. I., et al. 2019b, JGRA, 124, 7761

Wexler, D. B., Imamura, T., Efimov, A., et al. 2020a, SoPh, 295, 111

Wexler, D. B., Kooi, J. E., Jensen, E. A., & Song, P. 2022, FrASS, 9, 1047875

Woo, R. 1988, JGR, 93, 3919

Woo, R., & Armstrong, J. W. 1992, in Solar Wind, ed. E. Marsch & R. Schwenn (Goslar: Pergamon), 319

Woo, R., Armstrong, J. W., Sheeley, N. R., Jr., et al. 1985, JGR, 90, 154

Xu, G.-J., & Song, Z.-H. 2019, IEEE Wirel. Commun., 26-2, 10

Yuldashev, M. 2013, Mathematical Models and Simulation of Costas Loops (Jyväskylä: Univ. of Jyväskylä)

Zhang, Xi-Zhen 2007, ChJAA, 7, 712

Zheng, W.-M., MA, M.-L., & Wang, W.-B. 2013, Journal of Astronautics, 34, 1462

Zhu, X.-Y., Zhang, X.-Z., Zhang, H.-B., Kong, D.-Q, & Qu, H.-P. 2012, RAA, 12, 857